

Optical Engineering

OpticalEngineering.SPIEDigitalLibrary.org

Design, additive manufacturing, processing, and characterization of metal mirror made of aluminum silicon alloy for space applications

Enrico Hilpert
Johannes Hartung
Henrik von Lukowicz
Tobias Herffurth
Nils Heidler

SPIE.

Enrico Hilpert, Johannes Hartung, Henrik von Lukowicz, Tobias Herffurth, Nils Heidler, "Design, additive manufacturing, processing, and characterization of metal mirror made of aluminum silicon alloy for space applications," *Opt. Eng.* **58**(9), 092613 (2019), doi: 10.1117/1.OE.58.9.092613.

Design, additive manufacturing, processing, and characterization of metal mirror made of aluminum silicon alloy for space applications

Enrico Hilpert,^{a,*} Johannes Hartung,^a Henrik von Lukowicz,^{a,b} Tobias Herfurth,^a and Nils Heidler^a

^aFraunhofer Institute for Applied Optics and Precision Engineering IOF, High Performance Center for Photonics, Jena, Germany

^bFriedrich Schiller University of Jena, Institute of Applied Physics, Jena, Germany

Abstract. Metal mirrors are used for spaceborne optical systems, such as telescopes and spectrometers. In addition to the optical performance, the mechanical needs and the mass restrictions are important aspects during the design and manufacturing process. Using the additive manufacturing process, optimized internal lightweight structures are realized to reduce the weight of the system while keeping the mechanical stability. A mass reduction of $\approx 60.5\%$ is achieved. Using the aluminum silicon alloy AlSi40, the thermal mismatch of the mirror base body to a necessary electroless nickel-polishing layer is minimized. Based on an exemplary mirror design, the optimization of the interior lightweight structure is described, followed by the manufacturing process from additive manufacturing to diamond turning, plating, and polishing. Finally, the results of surface metrology and light scattering measurements are presented. A final form deviation below 80 nm *p. – v.* and a roughness of ~ 1 nm rms could be demonstrated. © The Authors. Published by SPIE under a Creative Commons Attribution 4.0 Unported License. Distribution or reproduction of this work in whole or in part requires full attribution of the original publication, including its DOI. [DOI: [10.1117/1.OE.58.9.092613](https://doi.org/10.1117/1.OE.58.9.092613)]

Keywords: optics; selective laser melting; metal mirror; mass reduction; aluminum 40 wt. % silicon.

Paper 190152SS received Feb. 1, 2019; accepted for publication Apr. 11, 2019; published online May 9, 2019.

1 Introduction

Modern telescopes and spectrometers for space applications require complex optical elements, such as aspherical or free-form surfaces, in order to meet the increasing requirements of optical designs. Metal optics are a good choice to accomplish the desired performance. The achievable quality of optical surfaces can even meet the requirements for extreme ultraviolet applications.¹ Optical systems for space applications are based on precise, mass-reduced, and stable assemblies of multiple mirrors to image the incoming beam with low aberrations onto a light-sensing element.^{2,3} Conventional manufacturing of the mirrors is limited in terms of achievable mass reduction and the possibility to tailor the mechanical properties. Additive manufacturing (AM) methods offer new concepts for the fabrication of metal optics, which can overcome the specific limitations of cutting technologies.^{4–6} Complex internal lightweight structures can be designed with a variety of configurations, such as periodical structures,^{5,7} honeycomb cells,⁴ and aperiodical or topology-optimized structures.⁵ The choice depends on the applied forces, the specified mechanical requirements, and the realizable complexity during the design process. Invar, beryllium, and aluminum alloys are state-of-the-art material systems for metal mirrors.⁸ Beryllium, aluminum, and also titanium alloys are of great importance for lightweight applications due to their high specific stiffness. Out of the given materials, aluminum is a good choice because in contrast to beryllium it is not hazardous, and it is easy to process and manufacture. However, the polycrystalline structure of aluminum prevents the generation of roughness values, which

are usable for visible and shorter wavelengths; a limitation, which is often countered by using an x-ray amorphous electroless nickel phosphorus (NiP)-polishing layer.⁹ The combination of an aluminum silicon alloy with 40 weight percent silicon (AlSi40) as substrate material and electroless nickel as plating is known to reduce bimetallic bending effect. This leads to a thermally stable design, which is based on the matching of the coefficient of thermal expansion between both materials in a temperature range of -185°C to 100°C .^{10,11}

The manufacturing of metal mirror base bodies using the selective laser melting (SLM) process with aluminum silicon material is described within this paper. SLM is an AM technique, which uses metal powder to generate parts by fusing successive layers that have been selectively illuminated by a laser. This includes complete melting and solidifying of the powder. SLM is applicable to process AlSi40 material and generate volume parts with a porosity of $<0.05\%$ using optimized process parameters.¹² The postprocessing after the AM process comprises a conventional machining to obtain the final geometry of the mirror base body and a first ultra-precise diamond turning process. After plating with electroless nickel, a second turning process is necessary. Final shape and roughness corrections are done by polishing methods such as magnetorheological finishing (MRF). The final optical surface is characterized by interferometric and light scattering measurements.

The article focuses on the AM-based manufacturing of a spherical single mirror (see Fig. 1) for the visual spectral (VIS) range with optimized interior structures, which yields a light and stiff mirror substrate. The lightweight structures are investigated and evaluated by using a finite element analysis (FEA), namely a so-called modal analysis, which seeks a solution to an eigenvalue problem and gives the

*Address all correspondence to Enrico Hilpert, E-mail: enrico.hilpert@iof.fraunhofer.de

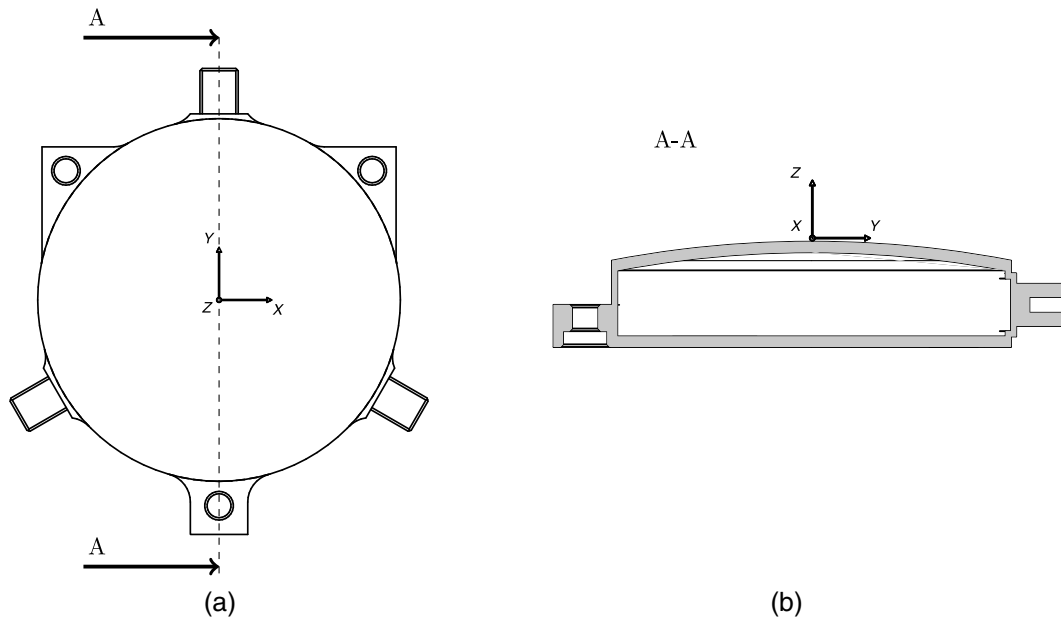


Fig. 1 Simplified mirror model with mounting structures every 120 deg around the circumference. The full aperture of the mirror measures 76 mm in diameter. The clear aperture is 72 mm in diameter. (a) View from top. (b) Cut through center with empty interior.

resonance frequencies of the part in question. This is a measure for the stiffness of a certain structure. For generation of the interior structures, the article focuses on so-called Voronoi cells,¹³ which are a dual pattern to a certain point distribution.

Different spatial frequencies of the surface deviation of the mirror are measured by an interferometer for the surface form deviation, white light interferometer for the surface roughness, and angular resolved scattering for comparison.

Therefore, the present article is organized as follows. In Sec. 2, the theoretical foundations of internal structures for mirror substrates are described and FEA are performed. The AM process for the mirror is described in Sec. 3. In Sec. 4, the diamond turning and postpolishing of the mirror substrate is discussed. Afterwards, the surfaces are characterized through a wide spatial frequency spectrum in Sec. 5. The article concludes with a summarized presentation of the results and shows a short outlook on the next steps in Sec. 6.

2 Theoretical Analysis

Since AM is a technology that allows for nontrivial internal structures of a part, one specific approach and its optimization are discussed in the following subsection. After that, the FEA of a part with newly developed internal structures is described. For analysis of the inner structure, an empty mirror model with 2 mm wall thickness is taken (see Fig. 1, right), whose interior is filled with four variations of this structure; a full model and an empty model are also analyzed by FEA as comparison.

2.1 Interior Optimization

Stable structures in biology are constituted in a way that they are optimized for certain load cases and low mass. Therefore, the optimization of internal structures begins by imitating biological structures. If one considers, e.g., the support cells of a bamboo stick its internal structure consists of quasi

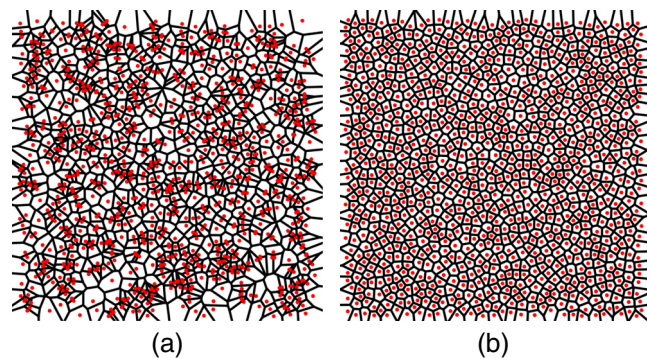


Fig. 2 Different sampling schemes and their corresponding Voronoi cells. (a) Uniformly distributed points showing an undesired clustering and therefore very asymmetric and deformed Voronoi cells. (b) Points sampled via a Poisson disk sampling showing very regular distributed and symmetric Voronoi cells.

randomly distributed nearly equi-sized cells. In this article, these are modeled by using a Voronoi cell pattern,¹³ which is generated by a random distribution of points. For this random distribution, it is not sufficient to choose the points in a uniform random manner since this leads to undesired clustering, see Fig. 2(a). A better approach is to use a certain distribution pattern that is also used in computer vision applications to obtain natural patterns. This is known as Poisson disk sampling,¹⁴ which is a so-called hard core process, denoting that the points have a strict lower value of nearest-neighbor distance and the process itself has a blue noise frequency characteristic, see Fig. 2(b).

After generating a Poisson disk point distribution and the appropriate Voronoi cells using Mathematica, these are transferred into the Surface Evolver software¹⁵ by utilizing the .fe file format. This software is used to obtain a minimum energy distribution with certain topological transitions that

are typical for dry foam. This leads to a structure that respects Plateau’s laws (e.g., Refs. 16–18), i.e.,

1. each face has constant mean curvature,
2. three faces meet at equal dihedral angles of 120 deg along cell edges,
3. four edges join at equal tetrahedral angles of $\arccos(-1/3) \approx 109.47$ deg at each cell vertex,

and is very stable due to its statistical nature. The structure generated for the model consists of straight lines, which means that the edges of the two-dimensional model optimized by the Surface Evolver were not further divided into segments.

For the Poisson disk sampling of the points, it is possible to provide a spatial function for the nearest-neighbor distance [see Fig. 3(b)] that assumes values between two limits. In order to make the interface to mounting structures more stiff, the radius function can be obtained by a fit from a topological optimization or an educated guess. This leads to a minimum energy foam configuration respecting the strain energy

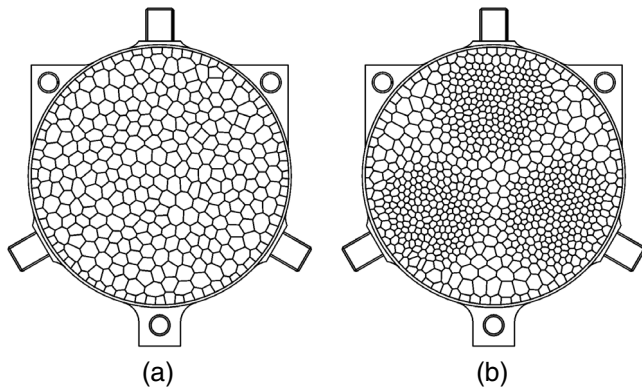


Fig. 3 Voronoi cells from Poisson disk sampling with different spatial functions for the nearest-neighbor distance. (a) Nearest-neighbor distance is kept constant. (b) In the three areas, the nearest-neighbor distance assumes smaller minimal values than in the surrounding area. The walls at the boundary are subject of fixed boundary conditions and therefore lead to a nearly perpendicular angle with respect to the outer wall. The interior cells were generated by using a start configuration of Voronoi cells and relaxing them via the Surface Evolver. The different “radii” of the cells were generated by different radii for the Poisson disk hard core process, which generated the point cloud on which the Voronoi cells are based.

distribution for certain load cases rendering the structure more stiff. Furthermore, the boundary conditions for Surface Evolver were set in a way that the walls of the outer cells are nearly perpendicular to the boundary structure, see also Fig. 3.

2.2 Finite Element Analysis

The finite element analyses were carried out by using ANSYS¹⁹ and extraction of frequency data from ANSYS text files was done by utilizing the computer algebra system Mathematica.^{20,21}

A convex mirror model (Fig. 1) was simulated by performing a modal analysis and extracting the first eigenmodes in a configuration where the mounting structures were fixed. This leads to a mechanically overconstrained system in which the estimation of the lower frequencies may be too conservative. But since all models are fixed by the same clamping, the differences between the models can be compared. The six analyzed mirror models are described in the following:

- “Full” model (a mirror without any interior light weight structure);
- “Empty” model (a mirror where the backside is closed but the interior is empty);
- “Two-dimensional (2-D) foam 0.7 mm” model (an interior structure according to Fig. 3(b) with 0.7-mm wall thickness);
- “2-D foam 0.5 mm” model (an interior structure according to Fig. 3(b) with 0.5-mm wall thickness);
- “2-D foam 0.5 mm equi” model (an interior structure according to Fig. 3(a) with 0.5-mm wall thickness);
- “2-D foam 0.3 mm” model (an interior structure according to Fig. 3(b) with 0.3-mm wall thickness).

In the modal analysis, the number of modes was calculated such that there are at least 85% of mean cumulated mass excited, which means 100 modes in the simulation are sufficient. The higher frequency excitations are useful to see to which extent the model reacts to the changed inner geometry due to the domination of the lower frequencies by the mounting.

Figure 4(a) shows the mean cumulative mode mass over frequency for the translational degrees of freedom. It is observed that the “full” model has nearly 95% excited mode mass at the fourth mode while the “empty” and “foam”

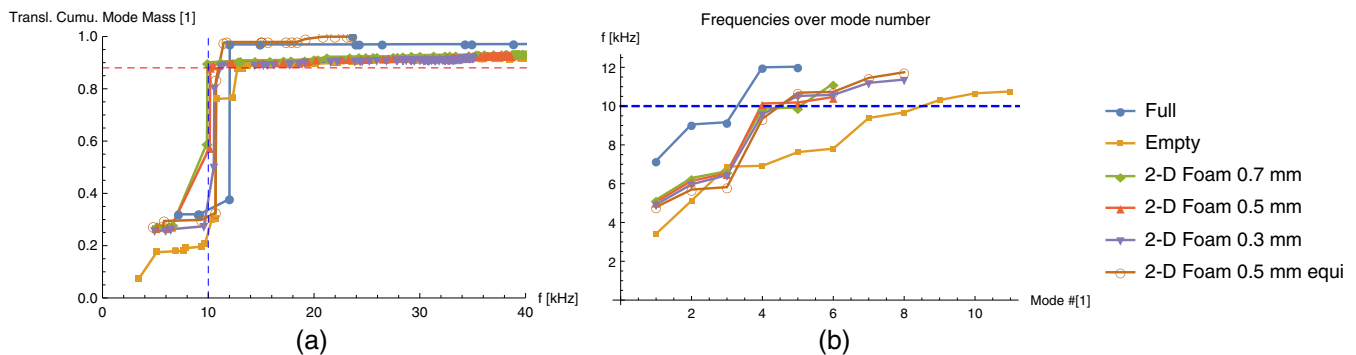


Fig. 4 (a) Mean cumulative mass for translational degrees of freedom over frequency. The blue dashed line denotes the 10-kHz shock load barrier and the red dashed line stands for the 88% cumulative mass limit. (b) Mode frequencies over mode numbers. The blue dashed line stands for the mentioned 10 kHz shock load barrier.

models, in contrast, exhibit an equal excitation at much higher frequencies.

The first eigenmode of the “full” model is excited at a higher frequency than at the “empty” model whereas the “foam” models show an intermediate behavior. This means on the one hand at lower frequencies the “full” model is better than the other models. On the other hand, for higher frequencies the situation turns around since the more lightweight models show more excited mode mass in the translational degrees of freedom in this frequency regime.

The number of modes appearing until the excited mode mass crosses either the 10-kHz shock limit (see Fig. 4 right) or the 88% cumulative mass limit is a “quality” indicator for the model. It can be observed that the “full” model crosses the 10-kHz limit after three modes whereas the “empty” model reaches the limit after eight modes. The “foam” models, again, show an intermediate behavior. Therefore, from a cumulative mode mass perspective, the “foam” models are a compromise between different “quality” indicators.

In Fig. 5, the first most relevant modes are shown, covering at least $\approx 82\%$ mean cumulative mode mass over all degrees of freedom. The plots show a decomposition of the

contributions of different degrees of freedom (translational and rotational) to the cumulative mode mass. Analysis of the bar plots gives the following picture:

- The “full” model has the most oscillating masses for each degree of freedom in the lowest six modes. The first mode is clearly dominated by 95% of the mass oscillating in t_z . The next two modes have 60% of the mass rotating in r_x and r_y . The fourth and fifth modes are dominated by 90% of the mass oscillating in t_x and t_y , respectively, while there are also small rotational parts. The sixth mode has 95% of oscillating mass in r_z .
- For the “empty” model, the oscillating masses are more widely distributed. The oscillation of the t_z degree of freedom is dominated by mode two, but mode one and mode nine are also dominated by an oscillation in t_z . Modes three to six are dominated by r_x and r_y oscillations. Some oscillating mass has r_x and r_y components in modes 10 to 13. Nearly, 70% of the oscillating mass in t_x and t_y are in the modes 10 and 11 and the rest oscillates in modes 12 to 15. The r_z

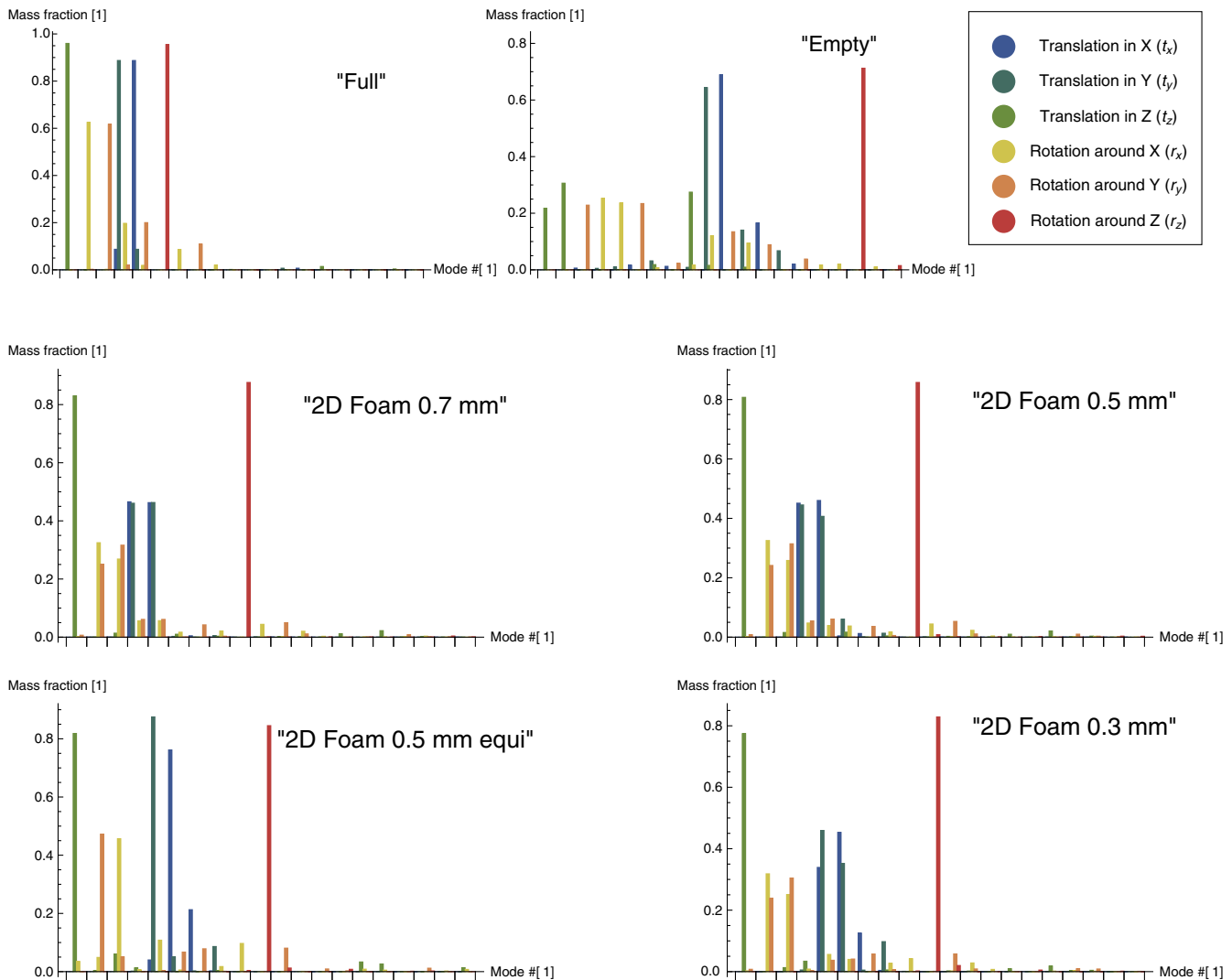


Fig. 5 Bar plots showing mass fraction for every degree of freedom (t_x , t_y , t_z , r_x , r_y , r_z) for every mode number at the six models under consideration.

degree of freedom oscillation clearly dominates mode number 18 with 70%.

- For the “foam” models “2-D foam 0.7 mm,” “2-D foam 0.5 mm,” and “2-D foam 0.3 mm,” all degrees of freedom are clearly separated by modes. The t_z degree of freedom clearly dominates the first mode. r_x and r_y dominate modes 2 and 3 and mix slightly into modes 4 and 5. t_x and t_y both contribute to modes 4 and 5 and the r_z degree of freedom dominates mode 9.
- Differences between the models “2-D foam 0.5 mm” and “2-D foam 0.5 mm equi” can be observed in modes 2 and 3 where there is a large asymmetry between r_x and r_y as well as modes 5 and 6 where there is a large asymmetry between t_x and t_y for the “2-D foam 0.5 mm equi” model. The mode mass fractions are also larger for the “2-D foam 0.5 mm equi” model than for the “2-D foam 0.5 mm” model.
- The simulation shows that all mode frequencies for the “full” model are higher than the respective mode frequencies of the other models, whereas those of the “empty” model are well below all other models. The “foam” models are situated between both extreme cases and are differing only slightly from each other.
- This means for the t_z degree of freedom: independent of the mode number the oscillation in z direction is excited first (from the frequency point of view) for the “empty” model, then, for the “foam” models, and still at higher frequencies for the “full” model. The same argument holds for the r_z degree of freedom.

In summary, it turns out that the “foam” models show an intermediate behavior between “empty” model and “full” model: a large portion of the mass is oscillating in the t_z degree of freedom in the first mode and a large portion of the mass is oscillating in the r_z degree of freedom in the ninth mode. The strengths are differing slightly between different wall thicknesses. Further, they are clearly superior in terms of stiffness and low excitation frequencies over the “empty” model. From a mass point of view, they are also superior to the “full” model and thus, a good compromise. Due to the slight changes in mass reduction factor and frequency properties for the “foam” models (see Table 1), it is not necessary to build the model with the thinnest walls. The comparison between the “2-D foam 0.5 mm” and “2-D foam 0.5 mm equi” shows that the size distribution of the cells plays an important role for mechanical stiffness. A customized layout was shown to be superior to a model with an equally sized cell pattern.

3 CAD Design and Additive Manufacturing of the Mirror Substrates

AM or 3-D printing is determined by the direct buildup of material based on computer aided design (CAD) data. The models have been created with PTC Creo 4.0 and exported

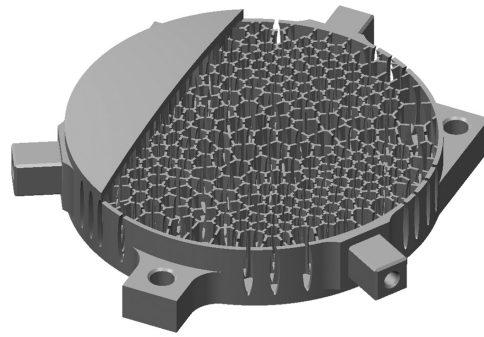


Fig. 6 Cut view of CAD model with interior lightweight structure. A: Mounting plane for first subsequent cutting process; B, C: mounting structures for fabrication and integration processes.

in STL format. The mechanical CAD model is shown in Fig. 6. The design is chosen to have a spherical optical surface with a curvature radius of 201.4 mm and a mechanical diameter of 76.0 mm. Mounting features are positioned in a 120-deg arrangement. Offsets of 1 mm at interface planes and functional surfaces are added to ensure enough material volume for subsequent cutting processes. The mirror substrate was designed using the interior structure of “2-D foam 0.5 mm” model shown in Fig. 3(b). All cells have connecting holes to each other and to the outer surface, respectively, see Fig. 6. The model with a wall thickness of 0.5 mm was chosen due to SLM process instabilities when aiming for structures thinner than this value. 0.5 mm walls are manufacturable and show a good compromise between process stability and lightweighting.

The final design realizes a mass reduction of 60.5% whereas the equidistantly sampled “2-D foam 0.5 mm equi” has slightly less mass with a mass reduction factor of 60.7% compared to a solid body design. Prior to the AM, the final CAD data have to be processed to be used on the SLM machine. This AM-related data processing includes the orientation of the CAD model within the building volume, the addition of supporting structure, and finally the slicing of the complete model into thin layers. In Fig. 7, the orientation and the added support structure are shown using the software “Materialise Magics.”

Transferring the sliced data onto the SLM machine (Concept Laser M2 Cusing), the physical buildup of the part can be accomplished. Figure 8 shows the schematic setup of the SLM machine. The metal powder is stored within the powder chamber, the buildup of the part takes place on the baseplate located in the building chamber. One layer of powder is coated onto the platform by lowering the building chamber, lifting the powder chamber, and moving the powder with the help of the coater from the powder to the building chamber. This new powder layer is illuminated by a laser beam, according to the data of the corresponding layer of the sliced model. The laser beam locally melts the powder and

Table 1 Mass reduction factors, given in percent.

Model	Full	Empty	2-D foam 0.7 mm	2-D foam 0.5 mm	2-D foam 0.5 mm equi	2-D foam 0.3 mm
lw^1	0.0%	70.8%	57.0%	60.5%	60.7%	64.3%

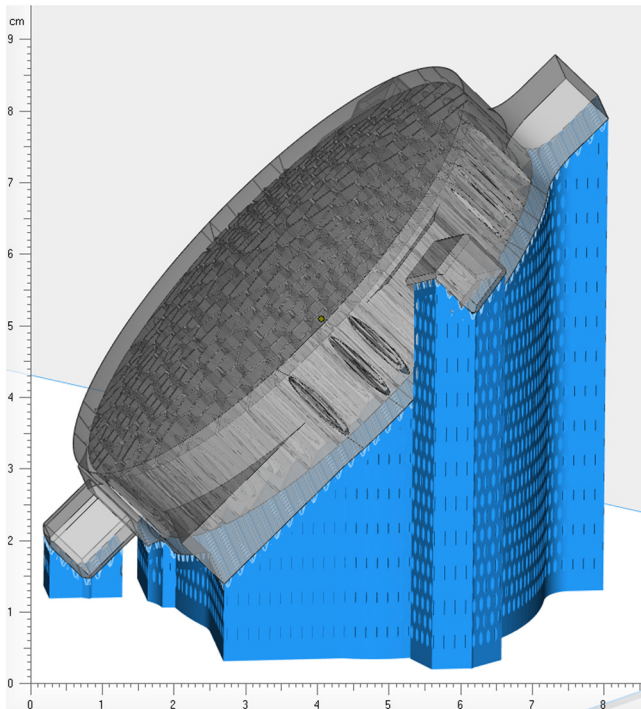


Fig. 7 Mirror model with support structure.

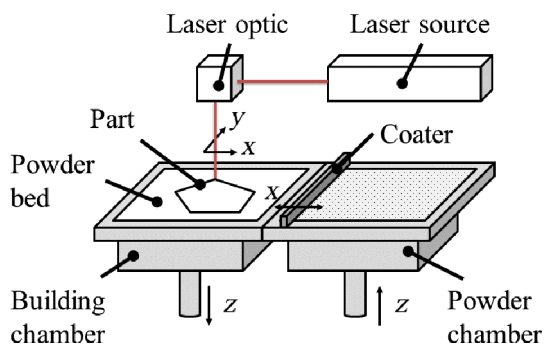


Fig. 8 Schematic setup of selective laser melting machine.

creates the solid metal volume. This procedure is repeated until the final part is stepwise built up to its final geometry.

To process the AlSi40 powder material, the SLM process parameters laser power and scanning speed were optimized to an energy input of 50 J/mm^3 . Using this value, a minimal porosity is achieved, the resulting value is below 0.05%. The building chamber is heated to 200°C during the SLM process to minimize internal stresses. After the build up by SLM is completed, the remaining powder is removed from the interior, followed by a stress relieving heat treatment. Finally, the mirror substrate is separated from the building platform and cleaned more thoroughly using an ultrasonic bath.

4 Ultraprecise Manufacturing and Postpolishing of Additively Manufactured Substrate

4.1 Cutting Fabrication and First Diamond Turning Step

The mechanical fabrication is carried out in several steps, so offsets are used to account for the material removal (or

addition, during electroless nickel plating) of each manufacturing process. In the following, negative numbers for the offsets denote measurements smaller than nominal where in contrast positive numbers indicate excess measurements. In general, the mounting surfaces are machined to close tolerances, reference surfaces are CNC machined leaving a remaining offset of $\approx -30 \mu\text{m}$. First, the mirror is mounted upside down with respect to plane A, see Fig. 6. The backside is then milled to the desired measure minus $\approx 30 \mu\text{m}$ offset. After that, the substrate is mounted using the generated backside as reference, also using the circumferential features. The features B and C (see Fig. 6) are then generated. These are necessary for mounting and integration into an optical system. After this step, the optical surface is milled. All other faces are not machined as this is not necessary. The manufacturing of the optical surface of the mirrors consists of several steps. First, the backside is flattened by lapping. The optical surface is then processed by ultraprecise (submicron accuracy) diamond turning. This generates the desired shape and removes an additional $\approx 10 \mu\text{m}$ of material, leaving an offset of $\approx -40 \mu\text{m}$. Turning was carried out on-axis using a monocrystalline diamond tool.

4.2 Electroless Nickel Plating

After the first diamond turning, the mirror substrate is coated with an electroless nickel layer of $\approx 55 \mu\text{m}$ thickness. The negative offsets are therefore removed, leaving around 10 to $20 \mu\text{m}$ positive offset for the remaining finishing operations. This layer consists of nickel with 10.5% phosphorus by weight and is therefore x-ray amorphous.²² This structure leads to a good machinability and enables polishing to very low roughness values.^{23–25} The coating is applied on all outer and interior surfaces to ensure good corrosion resistance and avoid electrochemical potential differences between NiP and AlSi40. After coating, the mirror substrate is cleaned and heat treated again to improve adhesion of the coating.

4.3 Finishing Operations

The remaining finishing operations include another diamond turning, followed by shape correction and smoothing techniques. The process chain for mirror manufacturing and its application to an additively manufactured mirror is shown in detail in Ref. 4. MRF is carried out to remove low frequency shape deviations and smoothen the surface. This technique is applicable to electroless nickel when customized fluids are used.²⁶ The roughness of the mirror substrates is finally addressed by a chemical mechanical polishing (CMP) technique. The polishing was carried out using an alkaline fluid with silicon carbide particles. For this procedure, the circumferential holes of the mirror substrate have been sealed in order to avoid contamination of the complex interior structure, which has already been cleaned. High pH polishing fluid was chosen because electroless nickel shows weaker corrosion resistance in this regime without tendency of pitting, which promotes the chemical part of the method.²² Figure 9 shows the shape deviation after the second turning [Fig. 9(a)] and MRF followed by CMP [Fig. 9(b)] in comparison. It can be seen that the remaining errors are greatly reduced; however, some midfrequency errors remain. Analyzing and correcting those parts of the surface deviation are under current investigation.^{27–31} The measurement is done using a Zygo interferometer, piston and tilt have been

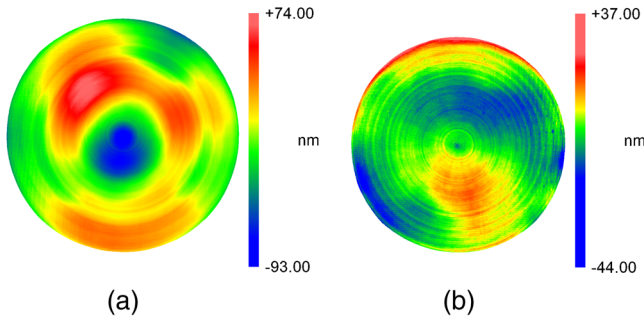


Fig. 9 Mirror shape deviation (a) after second diamond turning and (b) after the final CMP step.

removed from the data, and the aperture was set to 72 mm (therefore removing some edge effects from polishing). The remaining shape deviation after MRF is given by 68.6 nm *p. - v.* and 7.3 nm rms, and after a CMP step the values are slightly changed to 79.9 nm *p. - v.* and 7.3 nm



Fig. 10 Full-surface roughness and defect assessment using a light scattering sensor: photography of robot-guided scattering sensor and the sample.

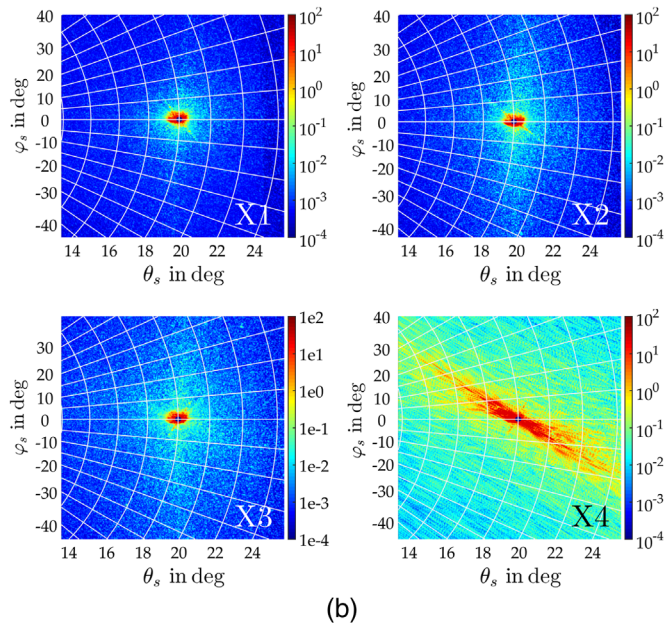
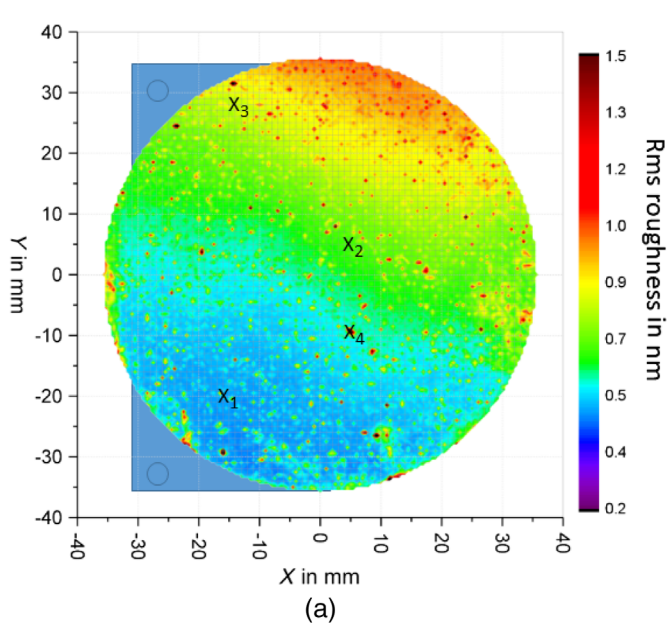


Fig. 11 Full-surface roughness and defect assessment using a light scattering sensor: (a) roughness and defect mapping. (b) ARS distributions, which correspond to the roughness evolution over the surface (X1 to X4). Right bottom: ARS of a defect or particle (X4).

rms. The roughness after diamond turning was measured using white light interferometry with a 50× magnification. This yields a measurement area of $140 \times 110 \mu\text{m}^2$ and a measured roughness value of 18.0 nm *p. - v.* and 2.9 nm rms. After CMP, the roughness was reduced to 9.5 nm *p. - v.* and 1.1 nm rms. As a final step, the mirror was coated with a layer of protected silver. This coating is applied for good reflectivity in the visible spectral range until near-infrared. The measured reflectivity of the completed mirror is between 95% and 98% in a wavelength range of 500 to 2500 nm.

5 Surface Metrology and Straylight

The roughness homogeneity as well as the distribution of contamination and defects on the mirror was assessed using a compact light scattering and roughness sensor.³²⁻³⁴ The robustness of the light scattering approach toward vibrations enables the combination of the sensor with an industrial robot (Universal Robots UR10), which provides the moving flexibility for full-surface characterization of aspherical or even freeform surfaces. More details on the robot based scattering sensor are discussed in Ref. 35. To achieve highly resolved roughness information over the entire surface, a raster scan with a local resolution of 0.5 mm was performed [Figs. 10 and 11(a)]. At each measurement position, an image of the angle resolved scattering (ARS)^{33,35} was recorded from which the local surface roughness in the spatial frequency range of about $f = 0.03$ to $0.3 \mu\text{m}^{-1}$ was calculated using Rayleigh-Rice theory.³⁵ Although the surface is coated with a protection layer, the calculations were performed using a single surface approximation of the protective coating.³⁶

The roughness mapping reveals an increasing roughness from the lower left with an average of about 0.5 nm to the top right with an average roughness of about 1 nm. The large number of singular increased roughness values corresponds to particles since the measurements were not performed in

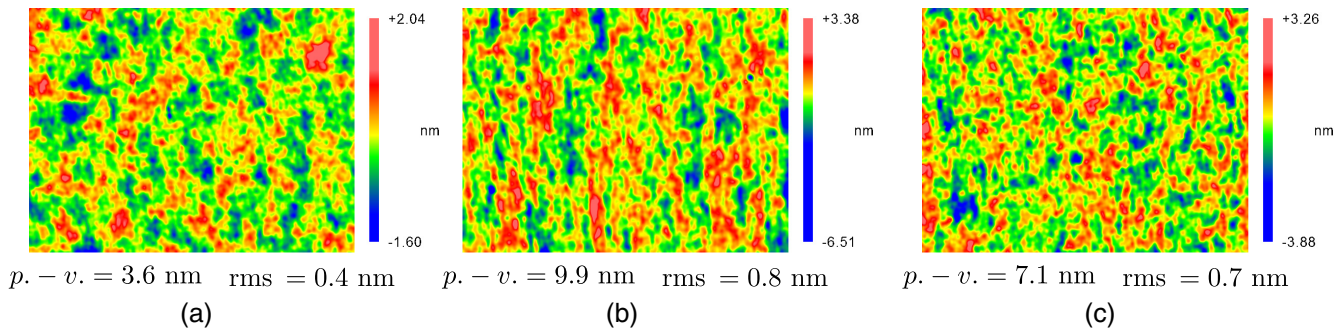


Fig. 12 WLI measurement of mirror at positions (a) X1, (b) X2, and (c) X3. Measurement area: $140 \times 110 \mu\text{m}^2$.

clean room environment. Exemplary scattering distributions, which show a section of about ± 8 deg of the scattering hemisphere around the specular reflected beam (wavelength: 660 nm; angle of incidence: 18 deg), are shown in the figure as well. The measurement positions X1 to X3 reveal that the roughness evolution is not caused by contamination since the changing vertical and nonisotropic scattering component show a fine granular speckle structure. This is not the case for typical localized particles or defects as at position X4. The roughness-induced anisotropic scattering corresponds to a stochastic but partially parallel structure on the surface, which might be induced by the MRF polishing process as described in Sec. 4. To validate the roughness map obtained by light-scattering, additional white light interferometry (WLI) measurements were done at the positions X1 to X3, see Fig. 12. To assure the comparability of these measurements, a band-pass filter is applied on the results of the WLI measurement to consider the spatial frequency range $f = 0.03$ to $0.3 \mu\text{m}^{-1}$ of the light scattering sensor. The slight increase of the roughness value from 0.4 to 0.8 nm rms can be confirmed by the WLI measurements. Without band-pass filtering, the roughness value is 1.3 nm rms. The shown roughness results could be used as an error map to realize an additional polishing step. However, for the presented proof-of-concept mirror, the obtained roughness is very good for imaging applications in the VIS spectral range.³⁷

6 Conclusions and Outlook

This study shows the fabrication of a mass-reduced mirror for applications of spaceborne optical systems. The design and optimization of the internal cell-like lightweight structures are presented. Using AM of aluminum with 40 wt. % silicon (AlSi40), the mirror base body was fabricated. Applying successive process steps such as diamond turning, plating with electroless nickel, and polishing steps, the roughness of the mirror was reduced to ~ 1 nm rms and a shape deviation of 80 nm $p. - v.$ was realized. The roughness measurement of the full surface was accomplished using a light scattering approach and confirmed by single white light interferometric measurements. It has been proven that the AM of the mirror base body is possible using AlSi40. The successive process steps can be applied leading to a mirror with optical characteristics for high end applications. The next steps will include the advancement to additive manufactured mirror bodies containing two mirrors on a common substrate as described in Refs. 2 and 3 and the

extension of AM to housings for optical systems such as telescopes or spectrometers. Here, the utilization of topology optimization during the design process can largely increase the weight reduction while keeping the mechanical and thermal performance of the housing. The final achievement will be the proof of the optical and mechanical performance of a telescope setup made by AM. A publication describing the results of this ongoing research is in preparation by the authors of this article, see Refs. 38 and 39 for some preliminary results.

Acknowledgments

The authors thank Matthias Beier, Andreas Gebhardt, Thomas Peschel, Stefan Risse, and Sven Schröder for very useful and enlightening discussions. They also thank Wilko Fuhlrott for diamond turning of the mirror, Knut Kleinbauer for MRF, Tom Pertermann for roughness and shape measurements, and Alexej Dmitriev for CMP. Further they thank Stephanie Hesse-Ertelt for helpful corrections. This work was funded by the Federal Ministry for Economic Affairs and Energy (Germany) under supervision of the German Aerospace Center (50EE1408). Acquisition of crucial equipment was realized with support from the Free State of Thuringia and the European Regional Development Fund (ERDF):

- SLM machine and equipment: Add-Light (14016-514).
- Polishing equipment: Frei-POL (2015FOR-0003)

References

1. T. Feigl et al., "Sub-aperture EUV collector with dual-wavelength spectral purity filter," *Proc. SPIE* **9422**, 94220E (2015).
2. M. Beier et al., "Development, fabrication, and testing of an anamorphic imaging snap-together freeform telescope," *Appl. Opt.* **54**, 3530–3542 (2015).
3. M. Beier et al., "Large aperture freeform VIS telescope with smart alignment approach," *Proc. SPIE* **9912**, 99120Y (2016).
4. E. Hilpert et al., "Precision manufacturing of a lightweight mirror body made by selective laser melting," *Precis. Eng.* **53**, 310–317 (2018).
5. H. Herzog et al., "Optical fabrication of lightweighted 3D printed mirrors," *Proc. SPIE* **9573**, 957308 (2015).
6. J. Mici et al., "Optomechanical performance of 3D-printed mirrors with embedded cooling channels and substructures," *Proc. SPIE* **9573**, 957306 (2015).
7. J. Kranz, D. Herzog, and C. Emmelmann, "Laser additive manufacturing of lightweight structures in TiAl6V4: a design for manufacturing approach," in *ESA Workshop Additive Manuf. Space Appl.*, Oral Presentation (2014).
8. A. Ahmad, *Handbook of Optomechanical Engineering*, CRC Press, Boca Raton, Florida (1997).
9. S. Risse et al., "Novel TMA telescope based on ultra precise metal mirrors," *Proc. SPIE* **7010**, 701016 (2008).

10. A. Gebhardt et al., "Athermal metal optics made of nickel plated AlSi40," *Proc. SPIE* **10563**, 105631J (2014).
11. J. Kinast et al., "Minimizing the bimetallic bending for cryogenic metal optics based on electroless nickel," *Proc. SPIE* **9151**, 915136 (2014).
12. E. Hilpert and S. Risse, "Additive manufacturing of aluminum alloy with high silicon content," in *Mater. Sci. Technol. Conf. and Exhib. (MS&T)* (2015).
13. G. F. Voronoy, "Nouvelles applications des paramètres continus à la théorie des formes quadratiques. premier mémoire. sur quelques propriétés des formes quadratiques positives parfaites," *J. Reine Angew. Math.* **1908**, 97–102 (1908).
14. A. Lagae and P. Dutré, "A comparison of methods for generating Poisson disk distributions," *Comput. Graphics Forum* **27**, 114–129 (2008).
15. K. Brakke, "Surface evolve website," 2013, <http://facstaff.susqu.edu/brakke/evolver/evolver.html> (14 December 2018).
16. J. A. F. Plateau, *Statique expérimentale et théorique des liquides soumis aux seules forces moléculaires*, Vol. 2, Gauthier-Villars, Paris (1873).
17. J. E. Taylor, "The structure of singularities in soap-bubble-like and soap-film-like minimal surfaces," *Ann. Math.* **103**, 489–539 (1976).
18. A. M. Kraynik, D. A. Reinelt, and F. van Swol, "Structure of random foam," *Phys. Rev. Lett.* **93**, 208301 (2004).
19. "ANSYS website," <https://www.ansys.com/> (18 July 2017).
20. S. Wolfram, *Mathematica: A System for Doing Mathematics by Computer*, 2nd ed., Addison-Wesley, Redwood City, California (1991).
21. S. Wolfram, *The Mathematica Book*, 5th ed., Wolfram Media, Champaign, Illinois (2003).
22. N. Kanani, *Chemische Vernicklung: Nickel-Phosphor-Schichten. Herstellung, Eigenschaften, Anwendungen. Ein Handbuch für Theorie und Praxis*, Eugen G. Leuze Verlag, Germany (2007).
23. J. W. Dini, "Perspective on plating for precision finishing," in *Am. Soc. Precis. Eng. (ASPE) Conf.*, Tucson, Arizona (1991).
24. A. Pramanik et al., "Ultra-precision turning of electroless-nickel: effect of phosphorus contents, depth-of-cut and rake angle," *J. Mater. Process. Technol.* **208**, 400–408 (2008).
25. J. Kinast et al., "Polishability of thin electrolytic and electroless NiP layers," *Proc. SPIE* **9633**, 963311 (2015).
26. M. Beier et al., "Fabrication of high precision metallic freeform mirrors with magnetorheological finishing (MRF)," *Proc. SPIE* **8884**, 88840S (2013).
27. T. Pertermann et al., "Angular resolved power spectral density analyses for improving mirror manufacturing," *Appl. Opt.* **57**, 8692–8698 (2018).
28. J. Stock et al., "Description and reimplementation of real freeform surfaces," *Appl. Opt.* **56**(3), 391–396 (2017).
29. G. W. Forbes, "Fitting freeform shapes with orthogonal bases," *Opt. Express* **21**, 19061–19081 (2013).
30. D. Aikens, J. E. DeGroot, and R. N. Youngworth, "Specification and control of mid-spatial frequency wavefront errors in optical systems," in *Front. Opt./Laser Sci. XXIV/Plasmonics and Metamater./Opt. Fabr. and Testing*, OTuA1 (2008).
31. T. Wang et al., "Controlling mid-spatial frequency errors in magnetorheological jet polishing with a simple vertical model," *Appl. Opt.* **54**, 6433–6440 (2015).
32. T. Herffurth et al., "Comprehensive nanostructure and defect analysis using a simple 3D light-scatter sensor," *Appl. Opt.* **52**, 3279–3287 (2013).
33. S. Schröder et al., "Device and method for angularly resolved scattered light measurement," Patent No. WO2010127872(A1) (2010).
34. M. Trost et al., "In situ and ex situ characterization of optical surfaces by light scattering techniques," *Opt. Eng.* **53**, 092013 (2014).
35. T. Herffurth et al., "Assessing surface imperfections of freeforms using a robotic light scattering sensor," *Opt. Eng.* **58**(9), 092609 (2019).
36. S. Schröder et al., "Spectral angle resolved scattering of thin film coatings," *Appl. Opt.* **53**, A35–A41 (2014).
37. M. Beier, "Fertigung und Kompensation von metalloptischen Hochleistungsspiegelsystemen für den visuellen Spektralbereich," PhD Thesis, Friedrich-Schiller-Universität Jena (2017).
38. J. Hartung, M. Beier, and S. Risse, "Novel applications based on freeform technologies," *Proc. SPIE* **10692**, 106920K (2018).
39. N. Heidler et al., "Additive manufacturing of metal mirrors for TMA telescope," *Proc. SPIE* **10692**, 106920C (2018).

Enrico Hilpert is materials scientist and PhD student at the Precision Engineering Department at Fraunhofer IOF. He received his Diploma (Dipl.-Ing.) degree in materials science from the Friedrich-Schiller-University of Jena in 2013 under the supervision of Andreas Bund. His current research interests include additive manufacturing, innovative materials and their mechanical properties, and process optimization.

Johannes Hartung is a theoretical physicist and scientist at the Precision Engineering Department at Fraunhofer IOF. He received his Diploma (Dipl.-Phys.) degree in 2009 and his PhD in theoretical physics in 2013 from Friedrich-Schiller-University of Jena. He has published several research papers in different areas such as gravitational theory as well as applied physics. His research interests include theoretical modeling, numerical simulations, and data analysis between optical and mechanical design, manufacturing, and metrology.

Henrik von Lukowicz is a mechanical engineer and PhD student at the Precision Engineering Department at Fraunhofer IOF. He has got a Diploma (Dipl.-Ing.) in aerospace engineering from the Technical University of Dresden. Prior to Fraunhofer IOF, he worked in the mechanical analyses departments of different space companies. Currently, he is involved in the mechanical development of topology optimized structures for space applications.

Tobias Herffurth graduated in physics in 2008 and received his PhD from the Friedrich-Schiller-University, Jena, in 2015. Since 2006, he has been with the Surface and Thin Film Characterization Group at the Fraunhofer IOF working on methods and applications for light scattering-based surface, defect, and thin film characterization.

Nils Heidler graduated in precision engineering in 2008 and received his PhD in mechanical engineering from the Technische Universität Ilmenau in 2015 under supervision of René Theska. His current research interests include additive manufacturing for optical applications and precision mechanical systems.